Title

EPR and Structural Characterization of Water-Soluble Mn^{2+}-Doped Si Nanoparticles.

Journal

The journal of physical chemistry. C, Nanomaterials and interfaces, 121(3)

ISSN

1932-7447

Authors

Atkins, Tonya M
Walton, Jeffrey H
Singh, Mani P
et al.

Publication Date

2017

DOI

10.1021/acs.jpcc.6b11000

Peer reviewed

THE JOURNAL OF PHYSICAL CHEMISTRY C

Article

pubs.acs.org/JPCC

EPR and Structural Characterization of Water-Soluble Mn^{2+}-Doped Si Nanoparticles

Tonya M. Atkins,[†] Jeffrey H. Walton,[‡] Mani P. Singh,[†] Shreyashi Ganguly,[†] Oliver Janka,[†] Angelique Y. Louie,[§] and Susan M. Kauzlarich*[,†]

[†]Department of Chemistry, [‡]NMR Facility and Biomedical Engineering Graduate Group, and [§]Department of Biomedical Engineering, University of California, Davis, One Shields Avenue, Davis, California 95616, United States

Supporting Information

ABSTRACT: Water-soluble poly(allylamine) Mn^{2+}-doped Si (Si_{Mn}) nanoparticles (NPs) were prepared and show promise for biologically related applications. The nanoparticles show both strong photoluminescence and good magnetic resonance contrast imaging. The morphology and average diameter were obtained through transmission electron microscopy (TEM) and high-resolution transmission electron microscopy (HRTEM); spherical crystalline Si NPs with an average diameter of 4.2 ± 0.7 nm were observed. The doping maximum obtained through this process was an average concentration of 0.4 ± 0.3% Mn per mole of Si. The water-soluble Si_{Mn} NPs showed a strong photoluminescence with a quantum yield up to 13%. The Si_{Mn} NPs had significant T_1 contrast with an r_1 relaxivity of 11.1 ± 1.5 mM^{-1} s^{-1} and r_2 relaxivity of 32.7 ± 4.7 mM^{-1} s^{-1} where the concentration is in mM of Mn^{2+}. Dextran-coated poly(allylamine) Si_{Mn} NPs produced NPs with T_1 and T_2 contrast with a r_1 relaxivity of 27.1 ± 2.8 mM^{-1} s^{-1} and r_2 relaxivity of 1078.5 ± 1.9 mM^{-1} s^{-1}. X-band electron paramagnetic resonance spectra are fit with a two-site model demonstrating that there are two types of Mn^{2+} in these NP's. The fits yield hyperfine splittings (A) of 265 and 238 MHz with significant zero field splitting (D and E terms). This is consistent with Mn in sites of symmetry lower than tetrahedral due to the small size of the NP's.

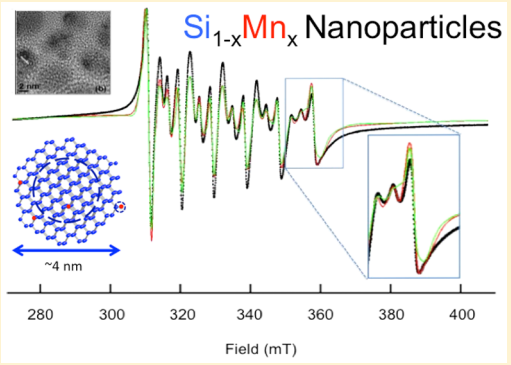

INTRODUCTION

There is a critical need for clinical probes that can simultaneously assist in early detection, diagnosis, imaging, and therapeutic treatment of disease.[1−3] Silicon NPs have been shown to have minimal toxicity and are easily passivated and inexpensive to produce.[4−7] Unlike the II−VI or III−V quantum dot (QD) materials, Si is a bioinert semiconductor that is electrochemically stable. Si nanoparticles have visible luminescence properties caused by a radiative recombination of an exciton (electrons and holes) in Si.[3,8,9] Free-standing luminescent Si nanoparticles have been prepared using a variety of physical and chemical techniques, including ultrasonic dispersion of electrochemical etching,[10] laser-driven pyrolysis of silane,[11] ion implantation,[12] synthesis in supercritical fluids,[13] metal−organic chemical vapor deposition (MOCVD),[14] pulverizing and sonicating p-Si,[15,16] and solution-based precursor reduction.[17−20] Significant advances in the preparation of Si nanoparticles have been realized in the past two decades.[8] However, two important issues that remain are the reliance of many of the existing methodologies on specialized reagents or reactors and the need for hazardous HF to afford efficient control over particle size.[21] To date, only a few studies have reported the colloidal synthesis of water-dispersible Si nanoparticles,[12,22−28] and most of the studies report Si nanoparticles used solely for fluorescence imaging.[9,29]

Manganese-doped group IV semiconductors have attracted attention because of their relevance in current device technology.[30−33] Mn^{2+} ions have been proven to be a useful magnetic resonance (MRI) contrast agent for functional imaging[31] as a noninvasive diagnostic for detection of disease. The addition of paramagnetic Mn^{2+} to Si nanoparticles would allow combinations of optical detection with magnetic resonance imaging techniques[33] or magnetic separation.[32] Mn^{2+} ions are similar to other paramagnetic ions since they are capable of shortening the T_1 of water protons. In addition, Mn^{2+} can also have a T_2 effect, influencing the signal intensity by shortening the transverse relaxation time to produce negative contrast.[34,35] Mn^{2+} has potential as useful contrast agents and can be a valuable tool in obtaining more information to get detailed physiological and biochemical information from MRI.[36] Recently, we have reported that for biological applications dual-modality imaging methods have shown potential for significantly increased diagnostic accuracy compared to stand-alone imaging.[33] This has led to increasing interest in multifunctional materials that can be detected by both modalities.

Received: November 2, 2016
Revised: December 22, 2016
Published: December 22, 2016

DOI: 10.1021/acs.jpcc.6b11000
J. Phys. Chem. C 2017, 121, 1948−1956

Incorporating dopants into nanostructures is difficult due to their small size and large surface-to-volume ratio which is an effective barrier to impurity doping.[37] Also, the doping of either n- or p-type impurities can cause the quenching of the photoluminescence (PL) because of the efficient Auger interaction between photoexcited electron−hole pairs and carriers supplied by the dopant element.[38,39] Typically, for group IV semiconductors, homogeneous doping of Mn^{2+} is difficult, largely due to the extremely low solubility of Mn in crystalline group IV semiconductors near room temperature.[40]

Water-soluble Mn-doped silicon (Si_{Mn}) and Fe-doped silicon (Si_{Fe}) nanoparticles have been prepared and characterized for biological applications.[7,33,41,42] In the case of Si_{Mn} nanoparticles, a major challenge to synthesis has been the low molar ratio of Mn in the nanoparticles (≤0.05%).[42] In an effort to increase the concentration of Mn in the Si nanoparticle, we have employed manganese(II) acetylacetonate as the source of Mn. In this paper, we focus on the synthesis and characterization of the NPs and EPR characterization of the Mn site in water-soluble, paramagnetic Si_{Mn} nanoparticles. The concentration of Mn in Si_{Mn} NPs afforded by using the organic manganese salts is improved 10-fold over our previous reports.[33] Electron paramagnetic resonance (EPR) illuminates the location of Mn in the Si_{Mn} NPs. These Si_{Mn} NPs were passivated with dextran in order to reduce their overall surface charge and improve solubility in anticipation of *in vivo* bioapplications.[33,43,44] These dextran-coated Si_{Mn} NPs were shown to have potential as an effective T_2 contrast agent.

EXPERIMENTAL SECTION

Materials. Sodium hydride powder (NaH, 95%), silicon powder (Si, 99%), anhydrous manganese(II) acetylacetonate powder ($Mn(acac)_2$, 99.99%), and allylamine (C_3H_7N, 98%) were purchased from Sigma-Aldrich and were used without further treatment. Ammonium bromide (NH_4Br, ≥99.99%) and *N*,*N*-dimethylformamide (DMF, 99.8%) were purchased from Sigma-Aldrich and dried before use. Water was purified using a Nanopure analytical UV water system (18.0 MΩ cm, Barnstead). All manipulations were carried out under dry N_2 or Ar gas, in a glovebox, a tube furnace, or Schlenk line, using standard anaerobic and anhydrous techniques.

Preparation of Mn-Doped Na_4Si_4 Precursors. Different Mn-doped Na_4Si_4 precursors were prepared according to a modified previously published procedure from Na_4Si_4.[45] Mixtures of NaH, Si, and Mn powders with the molar ratios (m_{NaH}:m_{Si}:m_{Mn} = 1.9:(1 − x):x, and x = 1%, 3%, 5%, and 7%) and NaH, Si, and $Mn(acac)_2$ powders with the molar ratios (m_{NaH}:m_{Si}:m_{Mn} = 1.9:(1 − x):x, and x = 1%, 3%, and 5%) were mixed in a Spex 8000M mill. A tungsten carbide vial, two tungsten carbide balls (diameter of ∼1 cm), and one tungsten carbide ball (diameter of ∼5 mm) were used to mill the mixtures. The milling was performed for 1 h (using 15 min on, 15 min off intervals for a total of 30 min) to obtain a homogeneous powder, which was transferred back into the glovebox.

The mixtures (NaH, Si, and Mn powder and NaH, Si, and $Mn(acac)_2$) were placed into separate 1 mL alumina crucible boats using a second 1.5 mL alumina boat as a cover. The crucibles were placed into a quartz tube with stopcocks on both ends. The quartz tube was removed from the glovebox and placed in a horizontal tube furnace and connected to Ar flowing at 30 mL/min. The quartz tube was rapidly heated (180 °C/h) to 420 °C and maintained for 48 h followed heating at 180 °C/h to 500 °C and dwelled for an additional 24 h. After cooling to room temperature, the tube was transferred back into the glovebox where the black solid was extracted and stored.

Caution: NaH and Mn-doped Na_4Si_4 powder are highly reactive to moisture and must be handled under an inert atmosphere!

Preparation of Water-Soluble Mn-Doped Si Nanoparticles. A two-necked 500 mL Schlenk flask was placed into the glovebox, and $Na_4Si_{4-x}Mn_x$ (0.25 g, 4.9 mmol) and NH_4Br (0.50 g, 5.1 mmol) were added and taken to a Schlenk line. 250 mL of degassed DMF was added by cannula to the solid. The mixture was allowed to reflux overnight under an inert atmosphere. After the reaction mixture was cooled to room temperature, 2 mL of allylamine was added, and the reaction mixture was allowed to reflux vigorously overnight while stirring. This mixture was allowed to cool to room temperature, and the mixture was centrifuged. The supernatant, a yellow solution, was decanted into a round-bottom flask. The solvent was exchanged with nanopure water using a rotavap followed by dialysis against nanopure water to purify the product of any unreacted and excess salts present. The resulting orange viscous product was filtered through a syringe filter to remove any solid impurities and was utilized for further characterization and studies.

pH Stability Study. Sodium tetraborate decahydrate was used to prepare a borate buffer for the pH stability study. Hydrochloric acid and sodium hydroxide were added to adjust the pH from 3 to 10 for a total of eight samples. Thirteen microliters was added to 3 mL of each acid and base from pH 3 to pH 10. The particles were allowed to sit for 2, 4, 6, 8, 24, 48, and 96 h, and at each time point the absorbance and emission were recorded. The eight samples were placed in an incubator for 2, 4, and 48 h at 37 °C. Following the incubation the samples were placed in a sandbath at approximately 90 °C for 4 h. The absorbance and emission were recorded for these time points.

Characterization. The X-ray powder diffraction data were collected with a Bruker D8 Advance diffractometer using Cu Kα radiation (40 keV, 40 mA). The samples were ground into powders and measured using a commercial sample holder supplied by Bruker for air-sensitive materials or a quartz plate for the precipitates from the reactions. Data were collected on a rotating sample (15 rpm) from 20° to 80° (2Θ), with a step size of 0.019 44° and a step time of 20 s for the air sensitive and 2.4 s for the non-air-sensitive samples, respectively. Data acquisition was performed using the Bruker Command Center software. No standard was added to the measurements. MDI Jade was used for phase identification; full pattern fitting for the present and identified phases was performed using the FullProf Suite.[46] Elemental analysis was performed by ICP quadrupole mass spectrometers (ICP-MS, Agilent Technologies 7500ce). Transmission electron microscopy (TEM) was performed on a Philips CM-12, operating at 80 kV. TEM samples were prepared by dipping holey-carbon-coated, 400-mesh electron microscope grids into the aqueous solution of the product and drying them in air. High-resolution transmission electron microscopy (HRTEM) was carried out using a JEOL 2500SE Schottky emitter microscope operated at 200 kV with a Gatan multiscan camera associated with it. The images were captured using a Digital Micrograph software provided by Gatan Inc. Infrared spectra were obtained by dropping the liquid onto the plate of a Bruker optic GmbH alpha ATR-FTIR. Photoluminescence (PL) spectra were measured on a FluoroMax-3P

DOI: 10.1021/acs.jpcc.6b11000
J. Phys. Chem. C 2017, 121, 1948−1956

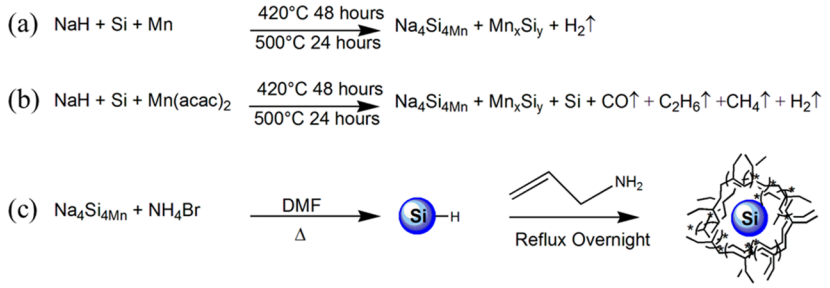

Figure 1. (a) Schematic representation of Mn-doped Zintl phase Na_4Si_{4Mn} with Mn metal powder. (b) Schematic representation of Na_4Si_{4Mn} with $Mn(acac)_2$. (c) Schematic representation of synthesis of poly(allylamine)-terminated Si_{Mn} NPs.

Table 1. Lattice Parameters of the Na_4Si_{4Mn} Samples

		lattice parameters				
preparation	% Mn added	a (Å)	b (Å)	c (Å)	β (deg)	V (Å^3)
ref 48	0	12.1536(5)	6.5452(5)	11.1323(6)	118.9(1)	775.26
A	1	12.1874(2)	6.5607(1)	11.1650(3)	119.018(1)	780.66
B	3	12.1999(2)	6.5691(2)	11.1706(4)	119.105(2)	782.20
C	5	12.2903(4)	6.5750(3)	11.0851(3)	118.905(2)	784.18

fluorometer, where the Mn-doped Si nanoparticles were dispersed in water.

Longitudinal (T_1) and transverse (T_2) relaxation times were measured at 60 MHz (1.4 T) and 37 °C on a Bruker Minispec mq60 (Bruker, Billerica, MA). The solutions of Mn-doped Si nanoparticles were prepared by dissolving appropriate amount of samples in pH 7.0 deionized water. T_1 values were measured using an inversion recovery sequence with 10−15 data points, and T_2 values were measured using a Carr−Purcell−Meiboom−Gill (CPMG) sequence with τ = 1 ms and 200 data points. Each solution was incubated at 37 °C for 10 min before measurement and measurements performed at 37 °C. The longitudinal (r_1) and transverse (r_2) relaxivity were determined as the slope of the line for plots of $1/T_1$ or $1/T_2$, respectively, against increasing manganese concentration with a correlation coefficient greater than 0.99.

Magnetic resonance imaging (MRI) was performed on a Bruker vertical bore 9.4 T (400 MHz) microimaging system, 21 °C, Bruker, Billerica, MA). The magnet was equipped with the standard gradient set (95 mT m^{-1} maximum gradient) and 25 mm internal diameter (i.d.) volume coil. Parameters for the images were TR = 500 ms and TE = 5 ms. For all images a flash-2D sequence was used with a field view (FOV) of 4.40 × 4.45 cm^2, slice thickness 1.0 mm, and a 128 × 128 matrix.

The electron paramagnetic resonance (EPR) spectra for the samples were collected on a Bruker ECS106 X-band spectrometer, equipped with an Oxford Instruments liquid helium cryostat. Typical experimental conditions were frequency 9.68 GHz, temperature 10 K, modulation amplitude 10 G, microwave power 63 μW, conversion time 40.96 ms, time constant 40.96 ms, resolution 2048 pts, and average of 10 scans. Samples were dissolved in dimethylformamide (DMF).

RESULTS AND DISCUSSION

Varying concentrations of Mn^{2+}-doped Si (Si_{Mn}) NPs were made by the reaction of the Mn-doped precursor Na_4Si_4 and NH_4Br in DMF and capped with poly(allylamine). Adapting a previously published procedure for M-doped Na_4Si_4, Na_4Si_{4M} (M = Mn, P, Fe),[41,45,47] mixtures of NaH, Si, and Mn metal powders or $Mn(acac)_2$ powders with different molar ratios were explored to determine if the Mn powder or a Mn complex would provide an increase of the Mn doping concentration thus leading to differing physical properties. The reaction equations are provided in Figure 1. Mn metal powder had been employed previously,[33] and in this study the $Mn(acac)_2$ complex is investigated as a potentially better starting material for Mn^{2+} incorporation. Three different starting concentrations of $Mn(acac)_2$ complex (1, 3, and 5%, noted as A, B, and C) were employed to produce Mn^{2+}-doped sodium silicide (Na_4Si_{4Mn}).[33] Figure 1b shows the reaction equation using the metal complex $Mn(acac)_2$. After reaching the final temperature of 500 °C, the main phase formed is Na_4Si_{4Mn}.

Powder X-ray diffraction was used to characterize Na_4Si_{4Mn} precursors (Supporting Information). Table 1 provides the lattice parameters for the main phase, Na_4Si_{4Mn}. As the amount of $Mn(acac)_2$ is increased, thermally stable binary manganese silicide phases are formed, and for the highest Mn content, a clathrate phase is observed in addition to Na_4Si_{4Mn}. The lattice parameters obtained for the three different preparations of Mn doping are consistently larger than that for pristine Na_4Si_4 (monoclinic, $C12/c_1$ (no. 15), a = 12.1536(5) Å, b = 6.5452(5) Å, c = 11.1323(6) Å, β = 118.9(1)°).[48] The volume increases from 780.66 Å^3 for preparation A to 784.18 Å^3 for preparation C; thus, we concluded that Mn^{2+} is incorporated into the structure of Na_4Si_4.

Si_{Mn} NPs are produced according to the reaction scheme in Figure 1c, and the resulting product is composed of two phases: a solid and liquid phase. The liquid phase is further purified while the precipitate is washed with methanol and characterized by X-ray diffraction. Although the precipitate is not used further, identifying the products in the precipitate provides insight into Mn^{2+} incorporation into the solution containing poly(allylamine)-coated Si_{Mn} NPs. The precipitate shows the presence of crystalline Si along with different manganese silicides and other phases (Supporting Information). The identified phases for the precipitate in all reactions are Si with increasing amounts of Mn_4Si_7. This seems reasonable since it can be observed from the Mn−Si phase diagram that manganese silicides are formed with an excess of either silicon or MnSi.[49] Table 2 provides the lattice parameters for the precipitated Si obtained in these reactions and shows that while

DOI: 10.1021/acs.jpcc.6b11000
J. Phys. Chem. C 2017, 121, 1948−1956

Table 2. Resulting Mn:Si (mol %) from the Nanoparticles in Solution from ICP-MS, Lattice Parameters of Si Precipitate from Powder X-ray Diffraction, and Quantum Yield (QY) of the Solution

		lattice parameters		
Mn:Si (mol %)	preparation	a (Å)	V (Å^3)	QY (%)
0.14 ± 0.04	C	5.4293(1)	160.04	13.2 ± 1.5
0.20 ± 0.1	A	5.4317(1)	160.25	11.1 ± 2.0
0.44 ± 0.3	B	5.4355(1)	160.59	13.1 ± 1.2

the lattice parameter increases for preparations A and B (1 and 3% Mn), it decreases for preparation C, the 5% initial composition of Mn^{2+}. This result suggests there is a threshold of how much Mn^{2+} can be incorporated into Si by this method. In addition to the lattice parameters, Table 2 provides the composition of the Mn^{2+} in the solution for the Si_{Mn} NPs. As the concentration of $Mn(acac)_2$ is increased from 1 to 5% in the Na_4Si_4 precursor, the highest concentration obtained for Mn in the Si_{Mn} NPs in solution was found to be 0.4 ± 0.3%. This is a 4 times greater Mn content compared to the nanoparticle product from Mn powder which yielded a maximum of 0.1 mol %.[33] The Mn complex allows for an increase in the Mn concentration in the NPs, which did not occur when using Mn powder. $Mn(acac)_2$ has the advantage of being more precisely weighed because of its molecular weight and better distributed in the Si powder via the ball milling than Mn metal powder which typically has a thin oxide coating. Since the sample is heated under flowing argon, the organic acetylacetonate is easily decomposed and removed from the sample. The lattice parameters obtained for the solid precipitate are consistent with the chemical analysis of the Si_{Mn} NP solution, suggesting that the highest Mn^{2+} content is for the materials preparation B with 3% $Mn(acac)_2$.

The morphology and size of Si_{Mn} NPs from $Mn(acac)_2$ (preparation B) were obtained by both low- and high-resolution TEM and EDS (Figure 2). In Figure 2a, the inset indicates a histogram from the high resolution data with the average diameter of 4.2 ± 1.0 nm, consistent with previously reported average sizes that are obtained from this reaction.[33,S0] The lattice fringes of 1.87 Å were consistent with the (220) silicon planes (Figure 2b). Lattice fringes measured from several HRTEM images verified that the NPs are diamond structured Si (Supporting Information, Figure 4). Selected area electron diffraction (SAED) is also consistent with crystalline Si (Figure 2c). Energy dispersive X-ray spectroscopy (EDS) (Figure 2d) provides further evidence confirming the presence of Si. However, Mn was not detected presumably due to the low concentrations within the NPs.

Figure 3 shows the FT-IR attenuated total reflectance (ATR) absorption spectrum of poly(allylamine)-coated Si_{Mn} NPs produced from the $Mn(acac)_2$ reaction. An N–H stretch is observed at 3393 cm^{-1} with CH_2 stretches at 3018 and 2929 cm^{-1}. An NH_2 deformation can be seen at 1660, 1640, and 1531 cm^{-1}. The C–N stretch is at 998 cm^{-1}, and the CH_2

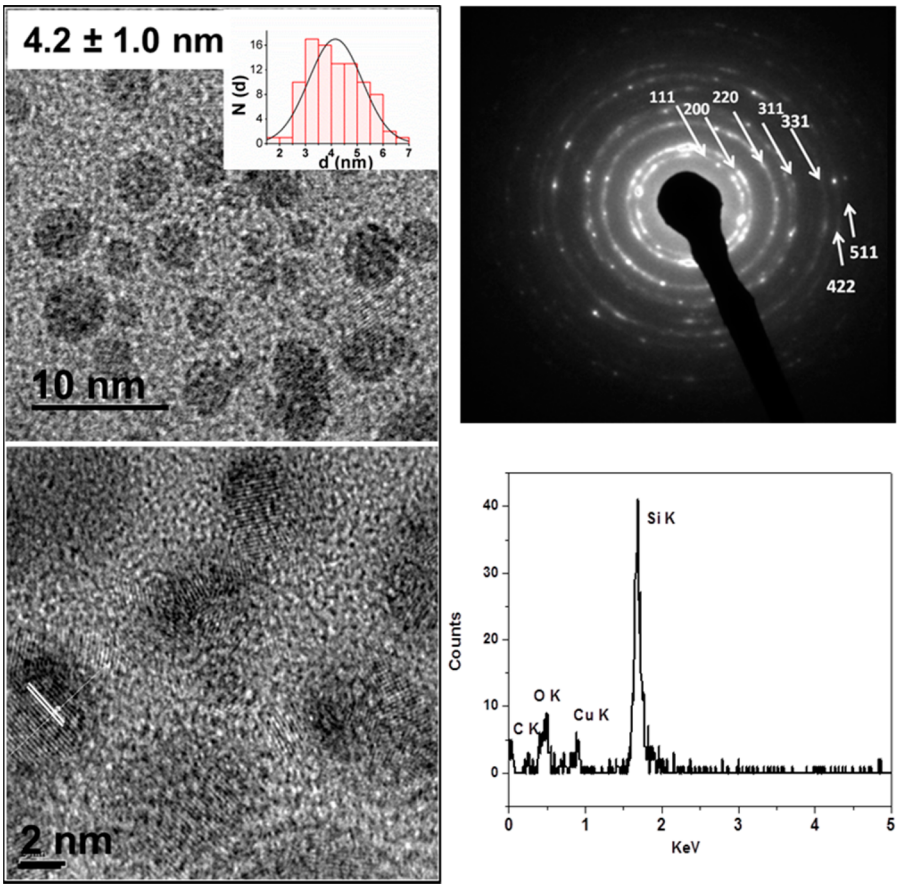

Figure 2. (a) TEM of Si_{Mn} nanoparticles preparation B with a histogram inset indicating an average size of 4.2 ± 1.0 nm. (b) High-resolution TEM showing the (220) lattice plane for Si. (c) SAED showing crystalline planes corresponding to Si. (d) EDS showing presence of Si.

DOI: 10.1021/acs.jpcc.6b11000
J. Phys. Chem. C 2017, 121, 1948–1956

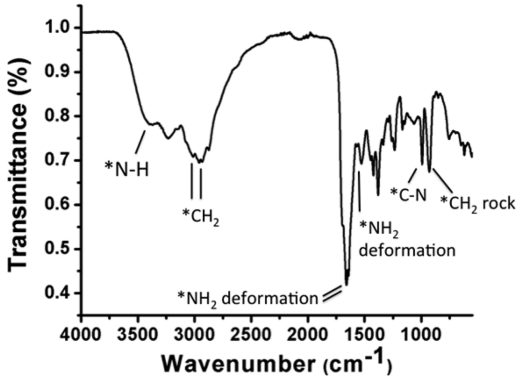

Figure 3. FT-IR ATR spectrum of poly(allylamine)-coated Si_{Mn} NPs.

rocking is at 934 cm^{-1}. This spectrum is similar to what is found in the literature for poly(allylamine).[51]

The pH and temperature stability of the Si_{Mn} NPs was tested. A photoluminescence study was used to determine possible decomposition based on a decrease in emission after treatment. The particles were allowed to sit for periods of time at increasing pH, and the emission was recorded. A quantum yield of 11−15% was observed (Supporting Information). In a second experiment, the samples were heated at 37 °C for periods of time and the quantum yield was maintained at 11−15%, suggesting high stability of the NPs. However, higher temperatures (90 °C) for 4 h resulted in a significant decrease in quantum yield to about 5%.

Figure 4 shows the T_1 and T_2 weighted MRI of phantoms of preparation B Si_{Mn} NPs and the optical emission of the same samples excited at λ_{ex} = 350 nm. The maximum emission is red-shifted and reduced as the concentration of the sample increased, indicating aggregation and quenching of the intensity. This result is similar to that observed for iron-doped Si, Si_{Fe}, NPs.[41] The intensities of the MRI phantoms demonstrate the brightening (top row) of T_1 weighted images and the darkening (bottom row) of T_2 weighted images vs concentration. Thus, Si_{Mn} NPs are both T_1 and T_2 relaxation agents and can be used in T_1 or T_2 weighted applications to deliver drugs coordinated in the polymer or conjugated through the amines for several different types of imaging. These data indicate that at least some of the Mn^{2+} ions are near the surface of the NP in order to relax water protons via inner- and outer-sphere mechanisms for T_1 weighted contrast. This is also consistent with EPR results (see below).

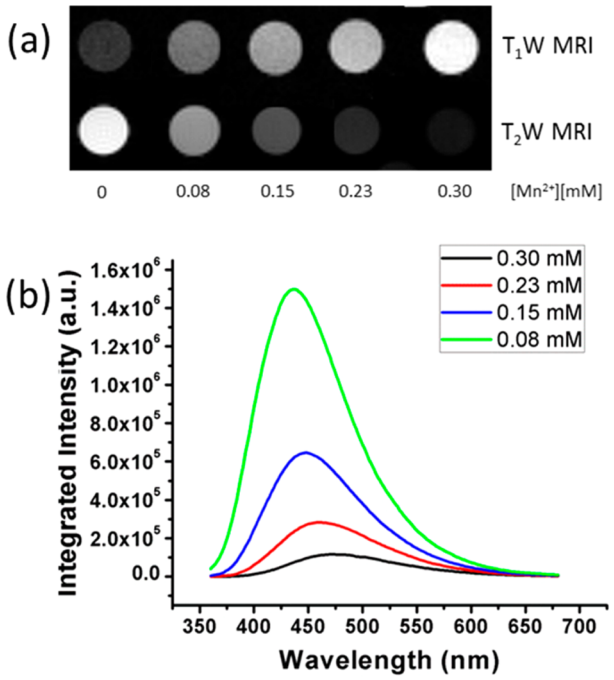

Figure 4. Si_{Mn} nanoparticles preparation B (0.4 ± 0.3 Mn:Si mol %), and concentrations are indicated for Mn^{2+}. (a) T_1 and T_2 weighted MRI of phantoms and (b) emission intensity measured at 350 nm.

Table 3 provides the Mn content in mol % (Mn:Si) and the measured relaxivities with and without dextran coating in mM per Mn^{2+}. The preparation label is the same as for Table 2; however, since we want to correlate the results with the amount of Mn^{2+} in the colloid, the order changes. Both Mn concentration and the dextran coating vary the relaxivities r_1 and r_2. The fits to the relaxation data vs concentration that yield the values in Table 3 are shown in the Supporting Information.

Previously reported samples of Si_{Mn} NPs equivalent to preparation A, but prepared using Mn metal powder to form Na_4Si_{4Mn}, were dextran sulfate coated and had an r_2/r_1 of 3.49 (with an r_1 relaxivity of 25.50 ± 1.44 mM^{-1} s^{-1} and an r_2 relaxivity of 89.01 ± 3.26 mM^{-1} s^{-1} with respect to [Mn^{2+}] (37 °C, 1.4 T)), indicating their use as a positive contrast agent.[33] Preparations B and C of Si_{Mn} NPs prepared with $Mn(acac)_2$ were chosen to be coated with dextran since the poly-(allylamine)-coated particles showed promising relaxivities. An r_1 relaxivity similar to the previously published results, 27.1 ± 2.8 mM^{-1} s^{-1}, was obtained but showed a larger r_2 relaxivity of 1078.5 ± 1.9 mM^{-1} s^{-1}. Likewise, preparation C showed similar results with a large r_2 of 822.4 ± 77.9 mM^{-1} s^{-1}.

The measured relaxivities are consistent with X-band electron paramagnetic resonance (EPR) results. EPR spectra of the NPs from the three preparations are shown in Figure 5.

These are classic looking Mn^{2+} EPR spectra with S = 5/2 and I = 5/2. The EPR spectra exhibit six large peaks that are the allowed ($\Delta m_S = \pm 1$) transitions, and the smaller doublets between are forbidden transitions ($\Delta m_S = \pm 1$ and $\Delta m_I = \pm 1$).[52] Several attempts at fitting the spectrum in EasySpin[53] were made.

Isotropic **A** and **g** tensors were used along with the zero field splitting parameters D and E (eq 1). Strain in D and E was also incorporated. The data cannot be fit with one component. To reproduce the long tails on either side of the lines requires a large amount of D strain. But large amounts of D strain overly broaden the sharp features. Thus, two component fits were attempted. We label the two components as type 1 and type 2. The EPR parameters g, A, [D E], [D strain E strain], and line width were varied, albeit not simultaneously. The two-component fits were significantly better than fitting only one component in every case, and for preparation C, a third spin 1/2 component was required. Figure 6 shows an example of the fit. In particular, the two-component fits reproduce the EPR spectrum significantly better in the region from 350 to 360 mT. The fits yielded a hyperfine coupling (A) value of ∼265 MHz for component type 1 for all three doping concentrations, which is similar to previously published results on Si-doped Mn^{2+} nanoparticles,[42] while for type 2, a value of ∼238 MHz was obtained. In the case of Mn^{2+} doping there was also a clear S = 1/2 signal at $g \sim 2$ in an initial data set taken with a 1 G field modulation (data not shown). The 10 G modulation used for acquiring the data for fitting diminishes the spin 1/2 signal

DOI: 10.1021/acs.jpcc.6b11000
J. Phys. Chem. C 2017, 121, 1948−1956

Table 3. Resulting Manganese Content in mol % (Mn:Si) and Measured Relaxivities per $[Mn^{2+}]$ with and without Dextran Coating of the Si_{Mn} NPs

		Si_{Mn} NPs		dextran-coated Si_{Mn} NPs	
Mn content (mol %)	preparation	r_1 (mM^{-1} s^{-1})	r_2 (mM^{-1} s^{-1})	r_1 (mM^{-1} s^{-1})	r_2 (mM^{-1} s^{-1})
0.14 ± 0.04	C	18.2 ± 3.6	211.0 ± 18.2	7.8 ± 0.3	822.4 ± 77.9
0.2 ± 0.1	A	0.40 ± 0.01	9.5 ± 1.0		
0.4 ± 0.3	B	11.1 ± 1.3	32.7 ± 4.2	27.1 ± 1.6	1078.5 ± 200.0

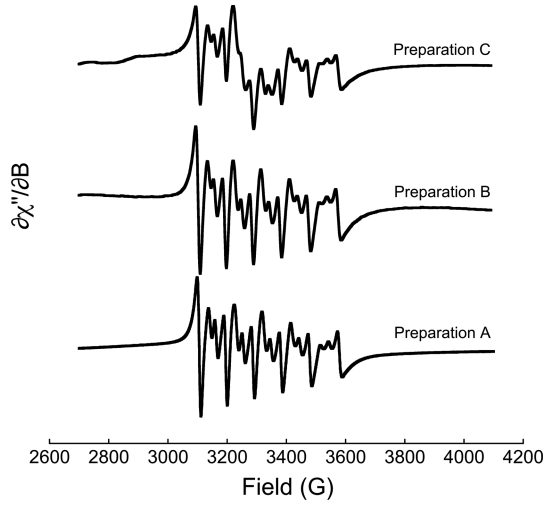

Figure 5. EPR spectra of the three different preparations A–C of Mn^{2+}-doped Si NPs, Si_{Mn}.

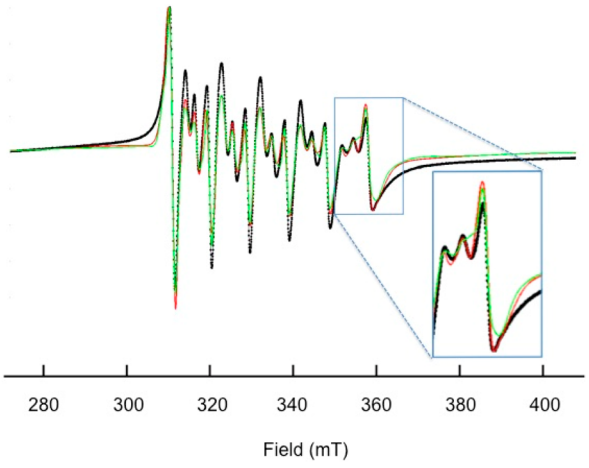

Figure 6. EPR data for preparation A Si_{Mn} NPs and fits. The data are shown in black, one-component fit is in green, and two-component fit is in red. Expanded view shows the feature that the two-component fit reproduces that the one-component fit does not.

to the point where it is not evident. Thus, a third species of spin 1/2 was also included in the fitting. These data are consistent with previous EPR on similarly prepared Si:Mn NP also acquired with 10 G modulation.[42] We attribute this signal to silicon dangling bonds. The fitting of the X-band data is very slow, indicating shallow minima in the least-squares fitting.

The EPR parameters of Mn^{2+} doped into Si take on a variety of values depending on sample preparation.[54−60,60−63] Both charge and spin state may be adjusted via doping, and each combination exhibits own hyperfine interaction. $S = 5/2$ is the natural state on Mn^{2+} in Si without doping, and $S = 5/2$ Mn^{2+} has been observed in Si in both interstitial and substitutional sites with $A = -160$ and -121 MHz, respectively.[58,63] Muller et al.[63] indicate that rapid quenching of transition metals in Si always produces interstitial type impurities. Substitutional Mn^{2+} is formed when vacancies annihilate with interstitial Mn^{2+}.[57] Note that the values for A obtained in Table 4 are about a factor of 2 larger than the studies cited above where Mn^{2+} is doped into single crystals but consistent with the previous report on Si_{Mn} NPs.[42]

Table 4. EPR and Relaxivity Parameters for the Three Preparations of Si_{Mn} NPs

	Mn content, mol % preparation		
parameters	0.14 ± 0.04 C	0.20 ± 0.1 A	0.44 ± 0.3 B
	type 1		
A (MHz)	264	266	264
[D E] (MHz)	[459 126]	[374 151]	[453 121]
[D E] strain (MHz)	[231 56]	[361147]	[251 41]
weight	4.4	6.8	3.8
	type 2		
A (MHz)	237	238	237
[D E] (MHz)	[925 −296]	[502 −65]	[894 −31]
[D E] strain (MHz)	[12 57]	[67 7]	[12 75]
weight	3.8	0.8	1.8
type 2 to type 1 ratio	0.86	0.12	0.46
r_1	18.2	0.4	11.1
r_2	211	9.5	32.7
dextran-coated r_1	7.8		27.1
dextran-coated r_2	822.4		1078.5

Both interstitial and substitutional sites have tetrahedral symmetry, and thus D and E terms are not expected unless there is deviation from that symmetry. Incorporation of the zero-field splitting (ZFS) accounts for the crystal-field-induced lowering from cubic (or higher) symmetry. This term can be expanded (to first order) as a function of two empirical parameters, D (the axial contribution to the ZFS) and E (the rhombic contribution):[52]

$$\vec{S}\hat{D}\vec{S} = D\left(\hat{S}_Z^{\,2} - \frac{S(S+1)}{3}\right) + \frac{E}{2}(\hat{S}_+^{\,2} + \hat{S}_-^{\,2}) \quad (1)$$

D and D strain (and thus E and E strain) were necessary for adequate fits and this is the first (that we know of) reported values of D and D strain in Mn-doped Si. We note that D and D strain have been used in fitting EPR spectra of Mn:CdSe quantum dots.[64] Previous studies of Mn doped into Si, which were performed on single crystalline Si, showed Mn doping levels several orders of magnitude lower than achieved here.[59] Thus, the Mn impurities were in sites of tetrahedral symmetry. Here, the small size (~4 nm diameter) of the particles would argue that a significant fraction of the Mn atoms are not in a site of tetrahedral symmetry due to being near the surface. Moreover, the high Mn concentration indicates there are

DOI: 10.1021/acs.jpcc.6b11000
J. Phys. Chem. C 2017, 121, 1948−1956

multiple Mn per NP (at 1% there are on average ~9.5 Mn atoms per NP). Furthermore, the standard theory for EPR parameters on Mn in Si demonstrates that next-nearest neighbors are important to the understanding of EPR spectra.[54] Thus, the existence of nearby electron spins in the form of another manganese and loss of tetrahedral symmetry for sites near the edge provide sufficient justification for the incorporation of D and E and their respective strains into the fits. Results are given in Table 4. These numbers are approximate as the fit minima are shallow. A high field EPR experiment would provide more definitive information.[64]

An important result from the fitting is that we obtain the relative amounts of the two types of sites. We note that for plain NPs there is a mild correlation between the type 2 to type 1 ratio and the r_1 relaxivity whereas there is a strong correlation between the type 2 to type 1 ratio and the r_2 relaxivity data (Table 4) but not measured Mn content. What is unclear from these data is the physical location of these two sites. There are several possible interpretations of this data. The first is that a "surface" type is increasing with the type 2:type 1 ratio, placing the magnetic moment closer to the water. We note that on a NP of 4.2 nm a shell of 0.4 nm (the Si next-nearest-neighbor distance) occupies approximately 1/4 of the volume of the NP. This suggests that the two sites could be from "surface" (in the outer shell) and "core". The high relaxivity argues for the larger fraction of type 2 Mn^{2+} to be near the surface. Furthermore, the D values obtained for type 2 are a factor of 2 larger than that of type 1, which is what one would expect if the Mn atoms are near the surface due to lower symmetry.

The relaxivity does not correlate with resulting Mn content. This lack of correlation of relaxivity with measured Mn content would be consistent with the correlation with type 2/type 1 ratio if the different preparations produced different distributions of Mn^{2+} within the NPs. Differences in average size of the NPs may also play a role, leading to different distributions of Mn^{2+}. Another possibility is that the spin 1/2 signal observed in preparation C is responsible for the large r_2.

r_1 and r_2 for the dextran-coated Si_{Mn} NPs both have a negative correlation with type 2:type 1 ratio but correlate with measured Mn^{2+} concentration. Of note is the particularly large r_2. The large r_2 combined with the ability to be further conjugated with target specific molecules makes them attractive for future bioapplications.

CONCLUSION

A higher percentage of Mn incorporation into Si nanoparticles was achieved by using $Mn(acac)_2$ to form the starting material, Na_4Si_{4Mn}. X-ray diffraction supports the claim that Mn is incorporated in the starting material, Na_4Si_{4Mn}, due to the increased lattice parameters. Incorporation of Mn into the Si_{Mn} NPs is assumed since the remaining precipitate consists of manganese containing phases. ICP analysis provides the amount of Mn and Si in the nanoparticle colloid. All samples maintained their photoluminescence and produced significant T_1 contrast. The Si_{Mn} NPs also show stability for extended periods of time throughout broad pH ranges. EPR indicates a two-component system where the Mn^{2+} ions occupy two different sites within the NPs and that the sites are of lower symmetry compared to Mn^{2+} doped into crystalline bulk Si. Moreover, since r_1 and r_2 are large, at least one type of Mn^{2+} is probably close to the surface. Characterization of the poly(allylamine)-coated Si NPs showed promising relaxivities for bioapplications. A next logical step is a surface modification with target specific molecules to probe the application in biological systems.

ASSOCIATED CONTENT

Supporting Information

The Supporting Information is available free of charge on the ACS Publications website at DOI: 10.1021/acs.jpcc.6b11000.

Figures of PXRD for Na_4Si_{4Mn} reagents and the precipitate from the reaction with NH_4Cl; a table with parameters from full pattern fitting of the PXRD; TEM images of the colloidal Si_{Mn} NP product; HRTEM of 3 mol % Si_{Mn} NPs with corresponding lattice planes indexed; plots of photoluminescence emission intensity as a function of pH, time, and heat for 3 mol % Si_{Mn} NPs; photoluminescence and UV−vis of 1, 3, and 5% Si_{Mn} NPs; relaxivity plots for colloidal Si_{Mn} NPs and dextran-coated Si_{Mn} NPs (PDF)

AUTHOR INFORMATION

Corresponding Author

*E-mail smkauzlarich@ucdavis.edu (S.M.K.).

ORCID

Oliver Janka: 0000-0002-9480-3888

Susan M. Kauzlarich: 0000-0002-3627-237X

Notes

The authors declare no competing financial interest.

ACKNOWLEDGMENTS

We recognize the support from NIH for funding this work through EB008576-01. NSF CRIF 1048671. The Bruker vertical bore 9.4 T (400 MHz) microimaging system was purchased on NIH Grant NIH S10 RR13871. We thank Drs. Xuchu Ma and Chuqiao Tu for their contributions to preliminary results and useful discussions.

REFERENCES

(1) Louie, A. Multimodality Imaging Probes: Design and Challenges. *Chem. Rev.* **2010**, *110*, 3146−3195.

(2) Howes, P. D.; Chandrawati, R.; Stevens, M. M. Colloidal Nanoparticles as Advanced Biological Sensors. *Science* **2014**, *346*, 1247390−1247390.

(3) Montalti, M.; Cantelli, A.; Battistelli, G. Nanodiamonds and Silicon Quantum Dots: Ultrastable and Biocompatible Luminescent Nanoprobes for Long-Term Bioimaging. *Chem. Soc. Rev.* **2015**, *44*, 4853−4921.

(4) Yong, K. T.; Law, W. C.; Hu, R.; Ye, L.; Liu, L. W.; Swihart, M. T.; Prasad, P. N. Nanotoxicity Assessment of Quantum Dots: From Cellular to Primate Studies. *Chem. Soc. Rev.* **2013**, *42*, 1236−1250.

(5) Park, J. H.; Gu, L.; von Maltzahn, G.; Ruoslahti, E.; Bhatia, S. N.; Sailor, M. J. Biodegradable Luminescent Porous Silicon Nanoparticles for in Vivo Applications. *Nat. Mater.* **2009**, *8*, 331−336.

(6) Ruizendaal, L.; Bhattacharjee, S.; Pournazari, K.; Rosso-Vasic, M.; de Haan, L. H. J.; Alink, G. M.; Marcelis, A. T. M.; Zuilhof, H. Synthesis and Cytotoxicity of Silicon Nanoparticles with Covalently Attached Organic Monolayers. *Nanotoxicology* **2009**, *3*, 339−347.

(7) Bhattacharjee, S.; Rietjens, I.; Singh, M. P.; Atkins, T. M.; Purkait, T. K.; Xu, Z. J.; Regli, S.; Shukaliak, A.; Clark, R. J.; Mitchell, B. S.; et al. Cytotoxicity of Surface-Functionalized Silicon and Germanium Nanoparticles: The Dominant Role of Surface Charges. *Nanoscale* **2013**, *5*, 4870−4883.

(8) Das, A.; Snee, P. T. Synthetic Developments of Nontoxic Quantum Dots. *ChemPhysChem* **2016**, *17*, 598−617.

DOI: 10.1021/acs.jpcc.6b11000
J. Phys. Chem. C 2017, 121, 1948−1956

(9) Peng, F.; Su, Y. Y.; Zhong, Y. L.; Fan, C. H.; Lee, S. T.; He, Y. Silicon Nanomaterials Platform for Bioimaging, Biosensing, and Cancer Therapy. *Acc. Chem. Res.* **2014**, *47*, 612−623.
(10) Belomoin, G.; Therrien, J.; Nayfeh, M. Oxide and Hydrogen Capped Ultrasmall Blue Luminescent Si Nanoparticles. *Appl. Phys. Lett.* **2000**, *77*, 779−781.
(11) Hua, F. J.; Erogbogbo, F.; Swihart, M. T.; Ruckenstein, E. Organically Capped Silicon Nanoparticles with Blue Photoluminescence Prepared by Hydrosilylation Followed by Oxidation. *Langmuir* **2006**, *22*, 4363−4370.
(12) Tilley, R. D.; Yamamoto, K. The Microemulsion Synthesis of Hydrophobic and Hydrophilic Silicon Nanocrystals. *Adv. Mater.* **2006**, *18*, 2053−2056.
(13) Holmes, J. D.; Ziegler, K. J.; Doty, R. C.; Pell, L. E.; Johnston, K. P.; Korgel, B. A. Highly Luminescent Silicon Nanocrystals with Discrete Optical Transitions. *J. Am. Chem. Soc.* **2001**, *123*, 3743−3748.
(14) Rowsell, B. D.; Veinot, J. G. C. Reductive Thermolysis of a Heterocyclic Precursor: A Convenient Method for Preparing Luminescent, Surfactant-Stabilized Silicon Nanoparticles. *Nanotechnology* **2005**, *16*, 732−736.
(15) Nayfeh, M. H.; Akcakir, O.; Belomoin, G.; Barry, N.; Therrien, J.; Gratton, E. Second Harmonic Generation in Microcrystallite Films of Ultrasmall Si Nanoparticles. *Appl. Phys. Lett.* **2000**, *77*, 4086−4088.
(16) Bley, R. A.; Kauzlarich, S. M.; Davis, J. E.; Lee, H. W. H. Characterization of Silicon Nanoparticles Prepared from Porous Silicon. *Chem. Mater.* **1996**, *8*, 1881−1888.
(17) Heath, J. R. A Liquid-Solution-Phase Synthesis of Crystalline Silicon. *Science* **1992**, *258*, 1131−1133.
(18) Dhas, N. A.; Raj, C. P.; Gedanken, A. Preparation of Luminescent Silicon Nanoparticles: A Novel Sonochemical Approach. *Chem. Mater.* **1998**, *10*, 3278−3281.
(19) Baldwin, R. K.; Zou, J.; Pettigrew, K. A.; Yeagle, G. J.; Britt, R. D.; Kauzlarich, S. M. The Preparation of a Phosphorus Doped Silicon Film from Phosphorus Containing Silicon Nanoparticles. *Chem. Commun.* **2006**, 658−660.
(20) Warner, J. H.; Rubinsztein-Dunlop, H.; Tilley, R. D. Surface Morphology Dependent Photoluminescence from Colloidal Silicon Nanocrystals. *J. Phys. Chem. B* **2005**, *109*, 19064−19067.
(21) Veinot, J. G. C. Synthesis, Surface Functionalization, and Properties of Freestanding Silicon Nanocrystals. *Chem. Commun.* **2006**, 4160−4168.
(22) Warner, J. H.; Hoshino, A.; Yamamoto, K.; Tilley, R. D. Water-Soluble Photoluminescent Silicon Quantum Dots. *Angew. Chem., Int. Ed.* **2005**, *44*, 4550−4554.
(23) Li, Z. F.; Ruckenstein, E. Water-Soluble Poly(Acrylic Acid) Grafted Luminescent Silicon Nanoparticles and Their Use as Fluorescent Biological Staining Labels. *Nano Lett.* **2004**, *4*, 1463−1467.
(24) Parak, W. J.; Gerion, D.; Zanchet, D.; Woerz, A. S.; Pellegrino, T.; Micheel, C.; Williams, S. C.; Seitz, M.; Bruehl, R. E.; Bryant, Z.; et al. Conjugation of DNA to Silanized Colloidal Semiconductor Nanocrystalline Quantum Dots. *Chem. Mater.* **2002**, *14*, 2113−2119.
(25) Wang, L.; Reipa, V.; Blasic, J. Silicon Nanoparticles as a Luminescent Label to DNA. *Bioconjugate Chem.* **2004**, *15*, 409−412.
(26) Sato, S.; Swihart, M. T. Propionic-Acid-Terminated Silicon Nanoparticles: Synthesis and Optical Characterization. *Chem. Mater.* **2006**, *18*, 4083−4088.
(27) Zhang, X. M.; Neiner, D.; Wang, S. Z.; Louie, A. Y.; Kauzlarich, S. M. A New Solution Route to Hydrogen-Terminated Silicon Nanoparticles: Synthesis, Functionalization and Water Stability. *Nanotechnology* **2007**, *18*, 095601.
(28) Erogbogbo, F.; Yong, K. T.; Roy, I.; Xu, G. X.; Prasad, P. N.; Swihart, M. T. Biocompatible Luminescent Silicon Quantum Dots for Imaging of Cancer Cells. *ACS Nano* **2008**, *2*, 873−878.
(29) Cheng, X. Y.; Lowe, S. B.; Reece, P. J.; Gooding, J. J. Colloidal Silicon Quantum Dots: From Preparation to the Modification of Self-Assembled Monolayers (Sams) for Bio-Applications. *Chem. Soc. Rev.* **2014**, *43*, 2680−2700.
(30) Zhang, Z. Z.; Partoens, B.; Chang, K.; Peeters, F. M. First-Principles Study of Transition Metal Impurities in Si. *Phys. Rev. B: Condens. Matter Mater. Phys.* **2008**, *77*, 155201.
(31) Lin, Y. J.; Koretsky, A. P. Manganese Ion Enhances T-1-Weighted Mri During Brain Activation: An Approach to Direct Imaging of Brain Function. *Magn. Reson. Med.* **1997**, *38*, 378−388.
(32) Leitsmann, R.; Kuwen, F.; Rodl, C.; Panse, C.; Bechstedt, F. Influence of Strong Electron Correlation on Magnetism in Transition-Metal Doped Si Nanocrystals. *J. Chem. Theory Comput.* **2010**, *6*, 353−358.
(33) Tu, C. Q.; Ma, X. C.; Pantazis, P.; Kauzlarich, S. M.; Louie, A. Y. Paramagnetic, Silicon Quantum Dots for Magnetic Resonance and Two-Photon Imaging of Macrophages. *J. Am. Chem. Soc.* **2010**, *132*, 2016−2023.
(34) Pan, D. P. J.; Schmieder, A. H.; Wickline, S. A.; Lanza, G. M. Manganese-Based Mri Contrast Agents: Past, Present, and Future. *Tetrahedron* **2011**, *67*, 8431−8444.
(35) Silva, A. C.; Bock, N. A. Manganese-Enhanced MRI: An Exceptional Tool in Translational Neuroimaging. *Schizophrenia Bull.* **2007**, *34*, 595−604.
(36) Koretsky, A. P.; Silva, A. C. Manganese-Enhanced Magnetic Resonance Imaging (Memri). *NMR Biomed.* **2004**, *17*, 527−531.
(37) Perego, M.; Bonafos, C.; Fanciulli, M. Phosphorus Doping of Ultra-Small Silicon Nanocrystals. *Nanotechnology* **2010**, *21*, 025602.
(38) Fujii, M.; Yamaguchi, Y.; Takase, Y.; Ninomiya, K.; Hayashi, S. Control of Photoluminescence Properties of Si Nanocrystals by Simultaneously Doping N- and P-Type Impurities. *Appl. Phys. Lett.* **2004**, *85*, 1158−1160.
(39) Delerue, C.; Lannoo, M.; Allan, G.; Martin, E.; Mihalcescu, I.; Vial, J. C.; Romestain, R.; Muller, F.; Bsiesy, A.; Auger. and Coulomb Charging Effects in Semiconductor Nanocrystallites. *Phys. Rev. Lett.* **1995**, *75*, 2228−2231.
(40) Zeng, L.; Huegel, A.; Helgren, E.; Hellman, F.; Piamonteze, C.; Arenholz, E. X-Ray Absorption Study of the Electronic Structure of Mn-Doped Amorphous Si. *Appl. Phys. Lett.* **2008**, *92*, 142503.
(41) Singh, M. P.; Atkins, T. M.; Muthuswamy, E.; Kamali, S.; Tu, C.; Louie, A. Y.; Kauzlarich, S. M. Development of Iron-Doped Silicon Nanoparticles as Bimodal Imaging Agents. *ACS Nano* **2012**, *6*, 5596−5604.
(42) Zhang, X.; Brynda, M.; Britt, R. D.; Carroll, E. C.; Larsen, D. S.; Louie, A. Y.; Kauzlarich, S. M. Synthesis and Characterization of Manganese-Doped Silicon Nanoparticles: Bifunctional Paramagnetic-Optical Nanomaterial. *J. Am. Chem. Soc.* **2007**, *129*, 10668−10669.
(43) Tu, C.; Ma, X.; House, A.; Kauzlarich, S. M.; Louie, A. Y. Pet Imaging and Biodistribution of Silicon Quantum Dots in Mice. *ACS Med. Chem. Lett.* **2011**, *2*, 285−288.
(44) Bhattacharjee, S.; de Haan, L. H. J.; Evers, N. M.; Jiang, X.; Marcelis, A. T. M.; Zuilhof, H.; Rietjens, I.; Alink, G. M. Role of Surface Charge and Oxidative Stress in Cytotoxicity of Organic Monolayer-Coated Silicon Nanoparticles Towards Macrophage Nr8383 Cells. *Part. Fibre Toxicol.* **2010**, *7*, 25.
(45) Ma, X. C.; Xu, F.; Atkins, T. M.; Goforth, A. M.; Neiner, D.; Navrotsky, A.; Kauzlarich, S. M. A Versatile Low Temperature Synthetic Route to Zintl Phase Precursors: Na4Si4, Na4Ge4 and K4Ge4 as Examples. *Dalton Trans.* **2009**, 10250−10255.
(46) Rodriguez-Carvajal, J. Recent Advances in Magnetic Structure Determination by Neutron Powder Diffraction. *Phys. B* **1993**, *192*, 55−69.
(47) Wang, J. L.; Sen, S.; Yu, P.; Browning, N. D.; Kauzlarich, S. M. Synthesis and Spectroscopic Characterization of P-Doped Na4si4. *J. Solid State Chem.* **2010**, *183*, 2522−2527.
(48) Goebel, T.; Prots, Y.; Haarmann, F. Refinement of the Crystal Structure of Tetrasodium Tetrasilicide, Na4si4. *Z. Kristallogr. - New Cryst. Struct.* **2008**, *223*, 187−188.
(49) Sadia, Y.; Gelbstein, Y. Silicon-Rich Higher Manganese Silicides for Thermoelectric Applications. *J. Electron. Mater.* **2012**, *41*, 1504−1508.
(50) Atkins, T. M.; Louie, A. Y.; Kauzlarich, S. M. An Efficient Microwave-Assisted Synthesis Method for the Production of Water

DOI: 10.1021/acs.jpcc.6b11000
J. Phys. Chem. C 2017, 121, 1948−1956

Soluble Amine-Terminated Si Nanoparticles. *Nanotechnology* **2012**, *23*, 294006.
(51) Rivas, B. L.; Seguel, G. V. Synthesis, Characterization of Poly(Allylamine)Chelates with Cu(Ii), Co(Ii) and Ni(Ii). *Polym. Bull.* **1996**, *37*, 463−468.
(52) Stich, T. A.; Lahiri, S.; Yeagle, G.; Dicus, M.; Brynda, M.; Gunn, A.; Aznar, C.; DeRose, V. J.; Britt, R. D. Multifrequency Pulsed Epr Studies of Biologically Relevant Manganese(Ii) Complexes. *Appl. Magn. Reson.* **2007**, *31*, 321−341.
(53) Stoll, S.; Schweiger, A. Easyspin, a Comprehensive Software Package for Spectral Simulation and Analysis in Epr. *J. Magn. Reson.* **2006**, *178*, 42−55.
(54) Ludwig, G.; Woodbury, H. Electronic Structure of Transition Metal Ions in a Tetrahedral Lattice. *Phys. Rev. Lett.* **1960**, *5*, 98−100.
(55) Ludwig, G. W.; Woodbury, H. H.; Carlson, R. O. Spin Resonance of Deep Level Impurities in Germanium and Silicon. *J. Phys. Chem. Solids* **1959**, *8*, 490−492.
(56) Woodbury, H.; Ludwig, G. Spin Resonance of Transition Metals in Silicon. *Phys. Rev.* **1960**, *117*, 102−108.
(57) Woodbury, H. H.; Ludwig, G. W. Vacancy Interactions in Silicon. *Phys. Rev. Lett.* **1960**, *5*, 96−97.
(58) Ludwig, G. W.; Woodbury, H. H. Electron Spin Resonance in Semiconductors. In *Solid State Physics*; Frederick, S., David, T., Eds.; Academic Press: 1962; Vol. *13*, pp 223−304.
(59) Weber, E. R. Transition-Metals in Silicon. *Appl. Phys. A: Solids Surf.* **1983**, *30*, 1−22.
(60) Kreissl, J.; Gehlhoff, W. Electron Paramagnetic Resonance of the Mn 40 Cluster in Silicon. *Phys. Status Solidi B* **1988**, *145*, 609−617.
(61) Martin, J.; Wedekind, J.; Vollmer, H.; Labusch, R. EPR Investigation of Manganese Clusters in Silicon. *Phys. Rev. B: Condens. Matter Mater. Phys.* **2000**, *61*, 1918−1923.
(62) Wedekind, J.; Vollmer, H.; Labusch, R. Tetrahedral Mn-I4 Cluster in Silicon. *Phys. Rev. B: Condens. Matter Mater. Phys.* **2001**, *63*, 233202.
(63) Muller, S. H.; Tuynman, G. M.; Sieverts, E. G.; Ammerlaan, C. A. J. Electron-Paramagnetic Resonance on Iron-Related Centers in Silicon. *Phys. Rev. B: Condens. Matter Mater. Phys.* **1982**, *25*, 25−40.
(64) Zheng, W. W.; Wang, Z. X.; Wright, J.; Goundie, B.; Dalal, N. S.; Meulenberg, R. W.; Strouse, G. F. Probing the Local Site Environments in Mn:Cdse Quantum Dots. *J. Phys. Chem. C* **2011**, *115*, 23305−23314.

DOI: 10.1021/acs.jpcc.6b11000
J. Phys. Chem. C 2017, 121, 1948−1956